MIT Open Access Articles

An analytical film drainage model and breakup criterion for Taylor bubbles in slug flow in inclined round pipes

Massachusetts Institute of Technology

An analytical film drainage model and breakup criterion for Taylor bubbles in slug flow in inclined round pipes

E. Lizarraga-Garcia[a,*], J. Buongiorno[b], M. Bucci[b]

[a]*Department of Mechanical Engineering, MIT, Cambridge, MA 02139, USA*
[b]*Department of Nuclear Science and Engineering, MIT, Cambridge, MA 02139, USA*

Abstract

The velocity of Taylor bubbles in inclined pipes is reduced if a lubricating liquid film between the bubble and the pipe wall is not present. An analytical model predicting the gravity-driven drainage of the lubricating film is presented in this article. The model is then used to establish a criterion for film breakup: if $\bar{t}_{bubble} = t_{bubble}/\tau < 0.01$ the thin film would not break up, where t_{bubble} is the bubble's passage time, and τ is the characteristic film drainage time based on the fluid properties, pipe geometry, and critical film thickness. The model is validated experimentally with Taylor bubbles in inclined pipes ($5°$ to $90°$, the latter being vertical) of stagnant liquids (ethanol, methanol, and mixtures of deionized water and methanol).

Keywords: Taylor bubble, slug flow, film drainage, film breakup criterion

1. Introduction

Flow of Taylor bubbles, also known as slug flow, is a common occurrence in wells, riser pipes and pipelines of crude oil and natural gas developments, as well as boiling-water nuclear reactors. Current predictive methods for this
5 flow pattern rely on the so-called mechanistic two-fluid model, where the flow is represented as a series of liquid slugs and Taylor bubbles [43, 30, 2, 32]. For the case of vertical pipes, an axisymmetric lubricating film with a constant

---

*Corresponding author
Email address:* `elizaga@mit.edu` (E. Lizarraga-Garcia)

thickness surrounds the Taylor bubble. For stagnant liquid, the range of the nondimensional film thickness, $\bar{h} = h/R$, where h is the film thickness and R is the pipe radius, is approximately $\bar{h} \in [0.08, 0.33]$ [23]. As the pipe inclination increases, the Taylor bubble approaches the pipe wall and the lubricating film becomes significantly thinner and non-axisymmetric; moreover, the thickness of the film decreases along the Taylor bubble due to azimuthal gravity-driven drainage (see figure 1). If the film breaks up, the surface tension force at the triple contact line reduces the velocity of the bubble significantly [3].

The existence of this lubricating film and its breakup have received some attention in the literature. Maneri and Zuber [25] and Hien and Fabre [14] studied the velocity of plane bubbles in two-dimensional ducts experimentally and numerically, respectively, using deionized (DI) water and methanol. They observed three different bubble shape regimes depending on the duct inclination: (i) the bubble touching the upper wall for $\theta \leq 60°$, (ii) a stable lubricating film where the bubble does not touch the duct for $\theta \geq 80°$, and (iii) an unstable transition region in between. Al-Safran et al. [1] observed a stable thin film at the top of the horizontal pipe in their slug flow experiments with high-viscosity fluids. However, these results are valid for the limited set of fluid properties and flow conditions explored in those studies. The drainage of a vertical film due to gravity was analyzed by Mysels et al. [28]; here we extend the analysis to the situation where the component of gravity in the direction of the flow varies continuously and surface tension may affect the dynamics [31].

In this article, a drainage model and breakup criterion for the lubricating film of Taylor bubbles in slug flow in inclined round pipes is presented. Such criterion can be used to determine under which conditions the lubricating film is present, which is a key input for both numerical simulations [15, 42, 4, 22] and mechanistic modeling of slug flow in order to determine correctly the Taylor bubble velocity and pressure drop. Also, it can be applied in flow assurance studies of high-viscosity oil slug flows, a critical aspect in oil and gas systems: corrosion of the pipe material causes its blockage, and antioxidants are added to the liquid to avoid it. The prediction of a liquid film above the Taylor bubble
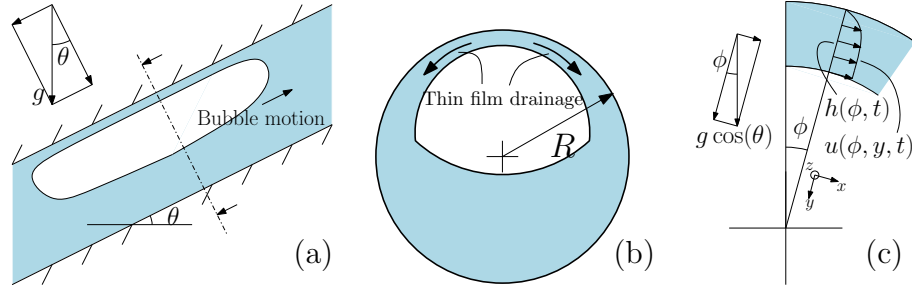
2

Figure 1: Taylor bubble and lubricating liquid film inside a round pipe with a θ inclination angle with respect to the horizontal (a), cross-sectional view (b), and coordinates used for the film drainage analysis (c). Not drawn to scale.

so that antioxidants touch the entire pipe is thus key to guarantee their safety.

2. Development of the thin film drainage and breakup model

2.1. Film drainage

Figure 1 shows the geometry and frame of reference chosen for the analysis of the lubricating liquid film drainage. Let u, v, and w denote the liquid film velocity in the azimuthal, radial, and longitudinal direction, respectively. Use of Cartesian coordinates is justified since $h/R \ll 1$. Thus, the Navier-Stokes equation in the x direction is

$$\rho \frac{\partial u}{\partial t} + \rho u \frac{\partial u}{\partial x} + \rho v \frac{\partial u}{\partial y} + \rho w \frac{\partial u}{\partial z} = -\frac{\partial p}{\partial x} + \mu \left(\frac{\partial^2 u}{\partial x^2} + \frac{\partial^2 u}{\partial y^2} + \frac{\partial^2 u}{\partial z^2} \right) + F_x(\phi), \quad (1)$$

where μ is the liquid viscosity, ρ is the liquid density, p is the pressure, $F_x(\phi) = \rho g \cos(\theta) \sin(\phi)$ where g is the gravity acceleration, and ϕ is the azimuthal angle with respect to the vertical. Equation 1 can be simplified using the lubrication approximation, by virtue of which various terms can be neglected:

$$\frac{\partial^2 u}{\partial x^2} \Big/ \frac{\partial^2 u}{\partial y^2} \quad \ll \quad 1, \qquad (2a)$$

$$\frac{\partial^2 u}{\partial z^2} \Big/ \frac{\partial^2 u}{\partial y^2} \quad \ll \quad 1, \qquad (2b)$$

$$\rho u \frac{\partial u}{\partial x} \Big/ \mu \frac{\partial^2 u}{\partial y^2} \quad \ll \quad 1, \qquad (2c)$$

$$\rho \frac{\partial u}{\partial t} \Big/ \mu \frac{\partial^2 u}{\partial y^2} \quad \ll \quad 1. \qquad (2d)$$

3

Note that equation 2c applies equally to the other two inertia terms of the equation after the continuity equation. Also, the pressure term can be neglected,

$$\frac{\partial p}{\partial x} \approx 0, \tag{3}$$

considering that the pressure differences inside the film due to gravity and surface tension are negligible, and the pressure inside the bubble is constant. Furthermore, the intermolecular forces are not included in equation 1. The validity of these approximations is verified in AppendixA. Thus, the previous Navier-Stokes equation 1 is simplified and, after imposing the non-slip at the wall and shear-stress-free at the film surface boundary conditions, the azimuthal film velocity profile is found:

$$u(\phi, y) = \frac{F_x(\phi)}{\mu} \left(hy - \frac{y^2}{2} \right), \tag{4}$$

a parabolic profile whose approximate shape is depicted in figure 1c. Similarly, the Navier-Stokes equation in the z direction is

$$\rho \frac{\partial w}{\partial t} + \rho u \frac{\partial w}{\partial x} + \rho v \frac{\partial w}{\partial y} + \rho w \frac{\partial w}{\partial z} = -\frac{\partial p}{\partial z} + \mu \left(\frac{\partial^2 w}{\partial x^2} + \frac{\partial^2 w}{\partial y^2} + \frac{\partial^2 w}{\partial z^2} \right) + F_z, \tag{5}$$

where $F_z = \rho g \sin(\theta)$. Note that v is much smaller than the other two velocity terms in this lubrication approximation. Following an analogous procedure as in the x direction, equation 5 is simplified and we obtain the longitudinal film velocity profile,

$$w(\phi, y) = \frac{F_z}{\mu} \left(hy - \frac{y^2}{2} \right). \tag{6}$$

In order to obtain the governing PDE for the film drainage, the continuity equation is used:

$$\frac{\partial h}{\partial t} + \frac{\partial Q'_x}{\partial x} + \frac{\partial Q'_z}{\partial z} = \frac{\partial h}{\partial t} + \frac{\partial}{\partial x} \int_0^h u dy + \frac{\partial}{\partial z} \int_0^h w dy = 0, \tag{7}$$

where Q'_x and Q'_z are the volumetric flow per unit length in the x and z direction, respectively. Using equations 4 and 6, and recognizing that $x = \phi \cdot R$, the second and third terms of the LHS of the previous equation can be developed:

$$\frac{\partial Q'_x}{\partial x} = \frac{\rho g \cos(\theta)}{\mu} h^2 \sin\left(\frac{x}{R}\right) \frac{\partial h}{\partial x} + \frac{\rho g \cos(\theta)}{3\mu R} h^3 \cos\left(\frac{x}{R}\right), \tag{8a}$$

$$\frac{\partial Q'_z}{\partial z} = \frac{\rho g \sin(\theta)}{\mu} h^2 \frac{\partial h}{\partial z}. \tag{8b}$$

Noting that the three RHS terms of the previous equations are positive, and $(\partial h/\partial z)/(\partial h/\partial x) \ll 1$ by scaling analysis it can be concluded that

$$\frac{\partial Q'_z}{\partial z} \ll \frac{\partial Q'_x}{\partial x}, \tag{9}$$

and therefore the film drainage PDE becomes

$$\frac{\partial h}{\partial t} + \frac{\partial}{\partial \phi}\left(\frac{\rho g \cos(\theta) h^3}{3\mu R}\sin(\phi)\right) = 0. \tag{10}$$

The initial and boundary conditions are

$$h(\phi, 0) = h_i(\phi), \tag{11a}$$

$$\frac{\partial h(0, t)}{\partial \phi} = 0, \tag{11b}$$

respectively, where equation 11b comes from the solution's symmetry at $\phi = 0$. An analytical solution for equation 10 can be obtained at $\phi = 0$ using the method of characteristics through the Lagrange-Charpit equations [8]. After some simple algebra, the thin film drainage at $\phi = 0$ is

$$h(\phi = 0, t) = \left(\frac{1}{h_0^2} + \frac{2\rho g \cos(\theta)}{3\mu R}t\right)^{-1/2}, \tag{12}$$

where $h_0 = h_i(\phi = 0)$. The evolution of the film thickness at $\phi = 0$, $h(\phi = 0, t)$, is key to determining when the film would break because that is the location of lowest thickness. To validate the analytical solution, equation 12 is compared with the numerical solution of equation 10 by a finite volume (FV) scheme implemented in MATLAB® [27] using 4th-order Runge-Kutta for the time marching, and the Lax-Friedrichs flux: Figure 2a shows they overlap perfectly for the high-viscosity oil whose properties are included in table 1. The nondimensional numbers used in table 1 are the Eötvös number $Eo = \rho g d^2/\sigma$, the Morton number $Mo = g\mu^4/(\rho\sigma^3)$, and the inverse viscosity number $N_f = \rho d^{3/2} g^{1/2}/\mu$, where d is the pipe diameter. Furthermore, it is important to note that $d\phi/dt \geq 0$ $\forall\, \phi \in [0, \pi]$ for the parameterized curve, which implies that the characteristics of the hyperbolic equation have positive slope and the information travels to the right along them, i.e., the right boundary does not affect the solution at
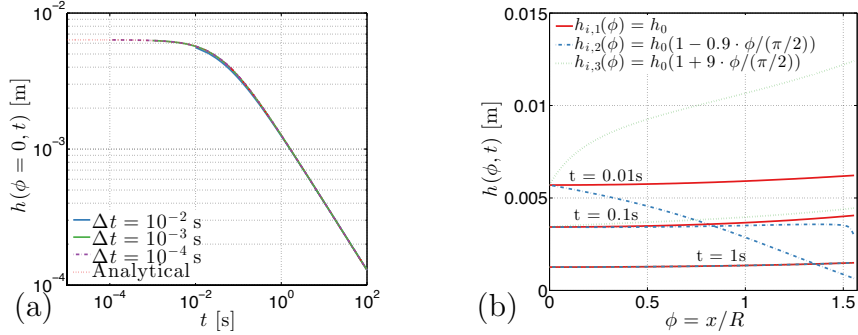
5

Figure 2: (a) Comparison of the analytical and numerical solutions of equation 10 for a high-viscosity oil at $\phi = 0$, where time convergence is done with three time steps. Note that the analytical and numerical solutions overlap perfectly. (b) Numerical solution for $\phi = [0, \pi/2]$ for three different initial film thickness, $h_{i,j}$, $j = 1, 2, 3$, at $t = 0.01$s, 0.1s and 1s. The film thickness at $\phi = 0$, $h(\phi = 0, t)$, is independent from the initial film thickness at $\phi > 0$, $h_i(\phi > 0)$.

Case	ρ [kg/m^3]	μ [Pa·s]	σ [N/m]	R [m]	Eo	Mo	N_f
kerosene	800	0.0016	0.028	0.025	700	$3.7 \cdot 10^{-9}$	17,500
high-viscosity oil	885	0.4	0.03	0.0254	750	8.4	84
water	999	0.001	0.072	0.0125	85	$2.6 \cdot 10^{-11}$	12,000

Table 1: Case study properties

$\phi = 0$. In particular, the solution for $h(\phi = 0, t)$ only depends on the initial condition at $\phi = 0$, $h_i(\phi = 0) = h_0$, and is independent from $h_i(\phi > 0)$. Figure 2b depicts the evolution of the numerical solution for the same high-viscosity oil for $\phi = [0, \pi/2]$ and three different initial film thickness, $h_{i,j}$, $j = 1, 2, 3$, where $h_{i,j}(\phi = 0) = h_0 \, \forall \, j$: a uniform film thickness, $h_{i,1} = h_0$; a linearly decreasing film thickness, $h_{i,2}(\phi) = h_0(1 - 0.9 \cdot \phi/(\pi/2))$; and a linearly increasing film thickness, $h_{i,3}(\phi) = h_0(1 + 9 \cdot \phi/(\pi/2))$. Three times are shown in the plot: $t = 0.01$s, 0.1s and 1s. The film thickness at $\phi = 0$, $h(\phi = 0, t)$, coincides for the three cases at all times, which shows that equation 12 is valid independently of the initial film thickness at $\phi > 0$, $h_i(\phi > 0)$.

6

2.2. Film breakup criterion in Taylor bubbles of slug flow

When the film drains to a critically low thickness, namely the critical thickness, h_c, it breaks. The breakup of liquid films between approaching particles and/or bubbles is an important step in coagulation processes in colloidal systems, e.g. the interaction of an air bubble with a solid particle in the industrial flotation processes in mineral processing, paper recycling and waste water treatment [37, 29, 26]. Two breakup mechanisms take place in wetting films [40, 38]: (i) capillary wave or spinoidal dewetting, and (ii) nucleation.

The capillary wave mechanism is based on classic hydrodynamic stability of the forces involved in the Derjaguin-Landau-Verwey-Overbeek (DLVO) theory, such as van-der-Waals and electrostatic double-layer interactions. Sheludko [39] derived the condition for kinetic instability of the film based on the capillary surface wave phenomenon. Vrij [47] obtained the critical wavelength, λ_c, in an explicit form, and derived two limiting expressions for the critical thickness, h_c, for negligible disjoining pressure with respect to the capillary pressure, and vice versa.

Nucleation refers to the presence of nanobubbles on a hydrophobic solid surface [16, 44, 17, 45, 24, 40, 41]. The mechanism here is similar to the film breakup in foam films, which has been extensively studied [7, 5].

In this context, fluids typically present in oil and gas systems and nuclear reactors wet the pipe surfaces, thus, the capillary wave mechanism applies.

Based on this critical thickness, h_c, equation 12 can be nondimensionalized:

$$\bar{h}(\phi = 0, \bar{t}) = \frac{h(\phi = 0, \bar{t})}{h_c} = \left(\left(\frac{h_c}{h_0} \right)^2 + \frac{t}{\tau} \right)^{-1/2} = \left(\left(\frac{h_c}{h_0} \right)^2 + \bar{t} \right)^{-1/2}, \quad (13)$$

where

$$\tau = \frac{3\mu R}{2\rho g \cos(\theta) h_c^2} \quad (14)$$

is the characteristic film drainage time. Figure 3 depicts the nondimensional gravity-driven film thickness evolution for three different combinations of initial and critical film thicknesses, h_0/h_c. The three lines overlap after a certain
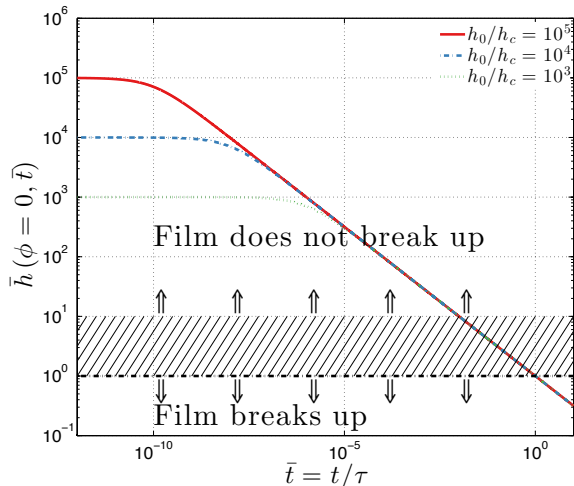
7

Figure 3: Film drainage and breakup map. The film is conservatively not broken while $h/h_c = \bar{h} > 10$.

time: an initial thicker film drains faster than a thinner one due to a higher gravitational force in comparison with the frictional one. Once they reach the same thickness, their drainage rate is the same. This can also be observed mathematically in equation 13, where $(h_c/h_0)^2$ becomes negligible with respect to the nondimensional time, $\bar{t}$.

As explained above, film breakup occurs when the film drains to h_c, i.e., when $\bar{h} = 1$. For the applications described in section 1, it is important to establish a criterion for the film to remain above the bubble. To be certain that the film is not broken, we can impose that the film thickness should be ten times bigger than the critical thickness, $h/h_c = \bar{h} > 10$. Based on equation 13 and figure 3, and assuming that $h_0/h_c > 10$, this is satisfied when the time the film is draining is lower than 0.01τ. At a given pipe cross section, the film at $\phi = 0$ drains while the bubble is passing below (see figure 1b). Thus, the film drainage time is equal to the bubble's passage time, t_{bubble}. Thus, the criterion to avoid film breakup in Taylor bubble flow becomes:

$$\bar{t}_{bubble} < 0.01. \tag{15}$$

8

In order to apply equation 15, the fluid properties, pipe geometry, and critical thickness are needed to calculate τ and the bubble's passage time. The critical film thickness can be estimated with the expressions of Vrij [47] and Sheludko [39], which characterize the capillary wave mechanism. Applying conservative estimates for the Hamaker constant, $h_c \sim 1$ μm is a conservative critical film thickness value for the typical fluids shown in table 1, high-viscosity oil, kerosene, and water, and steel pipe. The correlation of Llewellin et al. [23] for vertical pipes in stagnant liquid gives a film thickness, h, equal to 13, 2.4 and 0.67 mm, respectively. These numbers can be used to estimate the order of magnitude of the initial film thicknesses as $h_0 = h/10$, which are much larger than the estimated critical thickness. Finally, the Taylor bubble passage time can be estimated as the inverse of the slug frequency given by models of slug flow [10, 48, 9, 13], or by employing Taylor bubble velocity models [46, 11, 12, 20, 21] and an estimated length for individual bubbles.

3. Experimental validation

In order to validate the film drainage and breakup model, experiments of Taylor bubbles in inclined pipes of stagnant liquid are performed. There, the drainage time until the lubricating film breaks, $t_{breakup}$, is measured for different liquids and inclination angles (see figure 4). This breakup occurs when $\bar{h} = 1$. Based on equation 13, and assuming that $h_0/h_c \gg 1$, this corresponds to a nondimensional drainage time, $\bar{t}_{breakup}$, equal to 1, that is,

$$\bar{t}_{breakup} = \frac{t_{breakup}}{\tau} = \frac{t_{breakup}}{\frac{3\mu R}{2\rho g \cos(\theta) h_c^2}} = 1. \tag{16}$$

All the values of this equation but the breakup film thickness, h_c, are experimentally measured. Based on equation 16, the reported quantity

$$\frac{\bar{t}_{breakup}}{h_c^2} = \frac{t_{breakup}}{\frac{3\mu R}{2\rho g \cos(\theta) h_c^2} h_c^2} = \frac{t_{breakup}}{\frac{3\mu R}{2\rho g \cos(\theta)}} = \frac{1}{h_c^2} \tag{17}$$
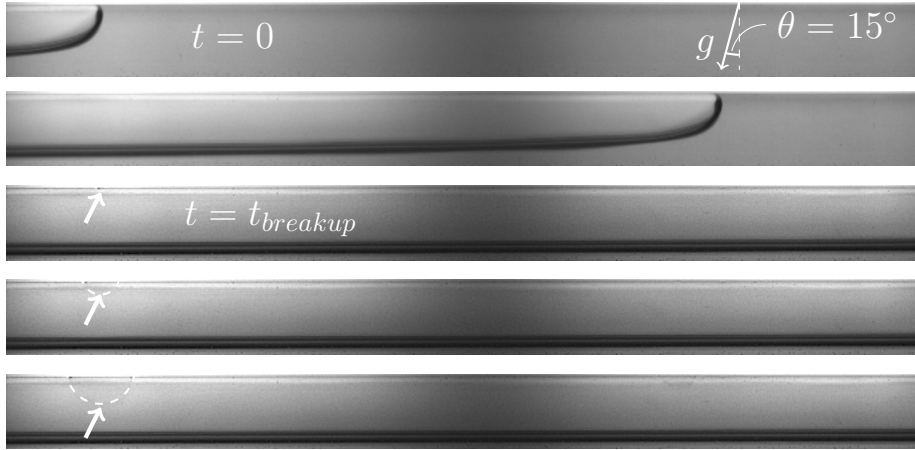
9

Figure 4: Example of the film breakup for a 50% DI water-50% methanol mixture at $\theta = 15°$ inclination. The shaded line indicates the film rupture front.

should be constant for every inclination angle and each liquid. Thus, an estimate of the film critical thickness can be obtained from the experimental measurements,

$$h_c = \sqrt{\frac{\frac{3\mu R}{2\rho g \cos(\theta)}}{t_{breakup}}}. \tag{18}$$

The experimental setup, shown in figure 5, consists of a High Speed Camera (HSC), a compressor, a polycarbonate tube of diameter $d = 0.0127$ m, and three valves. The inclination angles studied are $\theta = 5°$, $15°$, $30°$, $37.5°$, $45°$, $60°$, $75°$, and $90°$. The liquids used are methanol, ethanol, and three mixtures of DI water and methanol, whose properties are measured at the beginning and end of each experiment. These properties and the experimental techniques used are shown in table 2, where the mixture percentages are volumetric. The experimental procedure is as following: first, air at atmospheric pressure is held between the closed valves at "b" and "c". Then, valve "c" is opened and the Taylor bubble advances up through the tube due to gravity. The HSC records the bubble movement once it has reached its terminal velocity and generates the images shown in figure 4. The experiment finishes when the bubble reaches point "d". To rerun the experiment, the liquid contained between valves "b" and "c" is
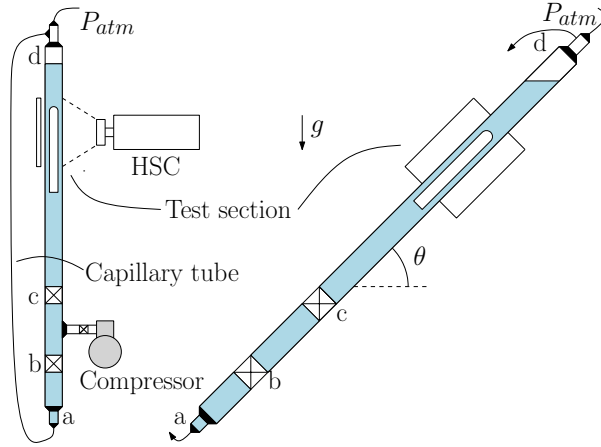
10

Figure 5: Experimental setup (not drawn to scale)

replaced by air at atmospheric pressure: the compressor pushes the liquid from "a" to "d" through the capillary tube while valve "c" is closed, and valve "b" opened. Since "d" is connected to atmosphere, compartment "b"-"c" remains at atmospheric pressure once the compressor is turned off. The closing of valve "b" confines the air at atmospheric pressure in this compartment so that the experiment can be performed again.

Five experiments are performed for each liquid and inclination angle. For certain liquids and inclination angles, film breakup does not occur and thus $t_{breakup}$ cannot be measured. In the present experimental setup, the film of ethanol and methanol does not break up at any inclination angle: both liquids wet polycarbonate effectively, as their contact angle values indicates in table 2, making the critical film thickness, h_c, low enough so that it is not reached during the gravity-driven drainage.

On the other hand, film breakup occurs for the mixtures of DI water and methanol. The HSC pictures of figure 4 show that the visually observable film breakup occurs at the top of the tube, $\phi = 0$, where the film is the thinnest, consistent with the present model. Table 3 reports the measured $\bar{t}_{breakup}/h_c^2$ values, the calculated h_c values (equation 18), and the maximum inclination angle at which breakup occurs, $\theta_{breakup,max}$, for each liquid. For the 50% DI water-50%

11

methanol mixture, film breakup occurs up to $60°$ inclination angle. For higher angles, the film does not drain enough to reach h_c and break. The values of $\bar{t}_{breakup}/h_c^2$ are scattered along an approximately constant value, as shown in figure 6. The experimental error, less than 10% the value of $\bar{t}_{breakup}/h_c^2$, is much smaller than the repeatability error, thus only the latter is reported. For the 37.5% DI water-62.5% methanol mixture, film breakup occurs only at 5 and $15°$ inclination angles, and the values of $\bar{t}_{breakup}/h_c^2$ are higher than those of the previous mixture, that is, the critical film thickness h_c is higher for the latter mixture, as inferred by its lower contact angle. Finally, the 25% DI water-75% methanol mixture only experiences film breakup at $5°$ inclination angle, and the value of $\bar{t}_{breakup}/h_c^2$ is again higher than the previous two mixtures, in accordance with its lower contact angle measured. The calculated critical thicknesses, h_c, are 24μm for the 25% DI water-75% methanol mixture, 35μm for the 37.5% DI water-62.5% methanol mixture, and 44μm for the 50% DI water-50% methanol mixture. The order of magnitude of these values coincides with the film thickness magnitude reported by Behafarid et al. [3], Podowski and Hirsa [33] and Podowski and Kumbaro [34], 50 to 100 μm, who studied theoretically and experimentally this phenomenon. Note that these values are slightly higher than the critical thickness estimation done in Section 2.3. The discrepancy is due to differences in the contact angle, which affects the film breakup mechanism and magnitude [40, 41]. The contact angle between the typical fluids of the systems mentioned (oil and gas, nuclear) and steel pipes, below $10°$ [6, 19], is much lower than in the experiments where the film breaks up, 40-$55°$. The experimental results have also been statistically analyzed: the Kolmogorov-Smirnov and Shapiro-Wilk tests state that the data $\bar{t}_{breakup}/h_c^2$ of each liquid follow a normal distribution around the mean shown in table 3.

4. Conclusions

In summary, it is important to predict under which conditions the lubricating film above a Taylor bubble in slug flow is present. In this article, an analytical

12

Liquid	ρ [kg/m^3]	μ [Pa·s]	σ [N/m]	Contact angle [°]
Ethanol	789	0.0011	0.022	0-5
Methanol	791.8	0.00058	0.022	1-5
25% DI water-75% Methanol	865.8	0.0014	0.024	40
37.5% DI water-62.5% Methanol	882.8	0.0015	0.025	45
50% DI water-50% Methanol	921.2	0.0018	0.031	55
Measurement technique	Calibrated volume weight	Capillary viscometer	Pending drop	Sessile drop

Table 2: Experimental liquid properties

Liquid	$\bar{t}_{breakup}/h_c^2$ [1/m^2]	h_c [μm]	$\theta_{breakup,max}$ [°]
Ethanol	-	-	-
Methanol	-	-	-
25% DI water-75% Methanol	1.7·10^9 (4·10^8)	24 (3)	5
37.5% DI water-62.5% Methanol	8.3·10^8 (2.1·10^8)	35 (5)	15
50% DI water-50% Methanol	5.2·10^8 (2.2·10^8)	44 (9)	60

Table 3: Experimental results, where values in parenthesis indicate standard deviation. Note that while h_c does not depend on θ, film breakup is not observed for $\theta > \theta_{breakup,max}$ as the film does not drain enough to reach that value.
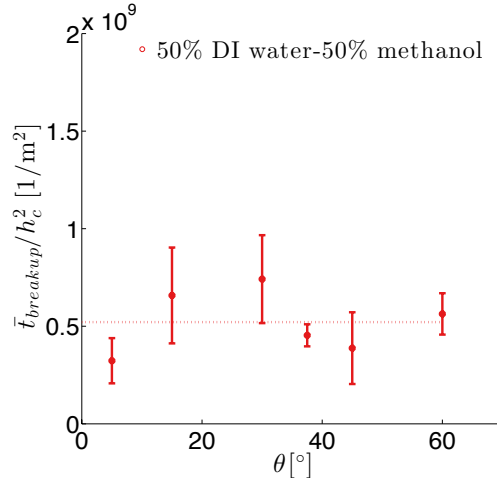
Figure 6: $\bar{t}_{breakup}/h_c^2$ values are scattered along an approximately constant value, from which the critical film thickness is calculated, $h_c = 44\mu m$.

model predicting the gravity-induced drainage of the thin film is presented, and from it a criterion to avoid the film breakup is derived: $\bar{t}_{bubble} = t_{bubble}/\tau < 0.01$. The model has been experimentally validated through Taylor bubbles in inclined pipes of stagnant liquids.

Acknowledgments

AppendixA. Approximations validity

The validity of the lubrication approximation (equations 2) and negligible pressure change inside the film (equation 3) and intermoluclar forces is proven

14

Case	Equation 2a	Equation 2b	Equation 2c	Equation 2d
kerosene	$2 \cdot 10^{-5}$	$2 \cdot 10^{-7}$	$5 \cdot 10^{-3}$	$7 \cdot 10^{-7}$
high-viscosity oil	$2 \cdot 10^{-5}$	$2 \cdot 10^{-7}$	$1 \cdot 10^{-7}$	$1 \cdot 10^{-11}$
water	$6 \cdot 10^{-5}$	$6 \cdot 10^{-7}$	$4 \cdot 10^{-2}$	$5 \cdot 10^{-6}$

Table A.4: Magnitude of the terms in equations 2 for the fluids of table 1, which justifies the lubrication approximation

here. Pipe geometries and fluids typical of slug flow such as high-viscosity oil, kerosene, and water (see table 1), are used to validate the lubrication assumptions (equations 2). In order to do so, the film thickness is scaled as one hundred times the critical film thickness $h \sim 100 h_c$; the bubble length is scaled as $10R$; the film velocity is scaled as the maximum velocity in the film at $y = h$ and $\sin(\phi) = \cos(\theta) = 1$, i.e., using equation 4 $u \sim (\rho g (100 h_c)^2)/(2\mu)$; and $\tau = (3\mu R)/(2\rho g \cos(\theta) h_c^2)$. The results reported in table A.4 confirm the accuracy of the lubrication approximation, equations 2.

In order to validate equation 3, the solution of the film thickness evolution accounting for the hydrostatic pressure and surface tension effects is successfully compared with the solution of equation 10. Also, the intermolecular forces are included through the intermolecular potential function in the liquid, Φ, accounting for the difference behavior between a thin film and a bulk liquid [35]. To include these effects, we first look at the Navier-Stokes equation in the y direction,

$$\rho \frac{\partial v}{\partial t} + \rho u \frac{\partial v}{\partial x} + \rho v \frac{\partial v}{\partial y} + \rho w \frac{\partial v}{\partial z} = -\frac{\partial (p + \Phi)}{\partial y} + \mu \left(\frac{\partial^2 v}{\partial x^2} + \frac{\partial^2 v}{\partial y^2} + \frac{\partial^2 v}{\partial z^2} \right) + F_y(\phi) + \sigma \kappa \delta (y - h),$$
$$(A.1)$$

where $F_y(\phi) = \rho g \cos(\theta) \cos(\phi)$, δ is the Dirac delta function, and $\kappa = h''/(1 + h'^2)^{3/2}$ is the curvature, where $h' = \partial h/\partial x$, and $h'' = \partial^2 h/\partial x^2$. Considering only van-der-Waals forces and neglecting electrical double layer interactions since there was no dilute electrolyte in the fluids studied, the intermolecular potential function, Φ, is

$$\Phi = \frac{A}{6\pi h^3}, \quad (A.2)$$

15

where A is the Hamaker constant which is negative when attractive [36]. As a conservative estimate, $A = -1 \cdot 10^{-19}$J in this study [18]. Since v is much smaller than the other two velocity terms in this lubrication approximation, the equation can be simplified to

$$0 = -\frac{\partial p}{\partial y} + F_y(\phi) + \sigma\kappa\delta(y - h). \qquad (A.3)$$

Equation A.3 can be integrated from y to h^+, where h^+ is located at the interface on the gas side:

$$\int_y^{h^+} \frac{\partial p}{\partial y} dy = \int_y^{h^+} F_y(\phi)dy + \int_y^{h^+} \sigma\kappa\delta(y - h)dy, \qquad (A.4)$$

that is

$$p_{gas} - p = F_y(\phi)(h - y) + \sigma h'', \qquad (A.5)$$

where $\kappa = h''/(1 + (h')^2)^{3/2} \approx h''$. Equation A.5 can be differentiated with respect to x:

$$\frac{\partial}{\partial x}(p_{gas} - p) = -\frac{\partial p}{\partial x} = F_y(\phi)h' - F_x(\phi)\frac{h - y}{R} + \sigma h''', \qquad (A.6)$$

where $h''' = \partial^3 h/\partial x^3$. The Navier-Stokes equation in the x direction, equation 1, is slightly modified by adding the intermolecular potential term, $\partial\phi/\partial x = -Ah'/2\pi h^4$. After some algebra, the azimuthal film velocity u becomes

$$u(\phi, y) = \frac{F_x(\phi)(1 - h/R) + F_y(\phi)h' + \sigma h''' - Ah'/2\pi h^4}{\mu}\left(hy - \frac{y^2}{2}\right) + \frac{F_x(\phi)}{2\mu R}\left(h^2 y - \frac{y^3}{3}\right), \qquad (A.7)$$

and the film drainage PDE is now

$$\frac{\partial h}{\partial t} + \frac{\partial}{\partial\phi}\left(\left(F_x(\phi)(1 - h/R) + F_y(\phi)h' + \sigma h''' - \frac{Ah'}{2\pi h^4}\right)\frac{h^3}{3\mu R} + F_x(\phi)\frac{5h^4}{24\mu R^2}\right) = 0. \qquad (A.8)$$

The initial and boundary conditions are the same as in equations 11. In order to solve equation A.8, a finite difference (FD) scheme is implemented in MATLAB® [27]. Matlab® ODE schemes for the time marching, and 2nd-order backward upwind schemes for the space derivatives are used. Figure A.7 shows the numerical solution of equation A.8 (where $\partial p/\partial x \neq 0$) at $\phi = 0$ and the

analytical solution (equation 12, $\partial p/\partial x = 0$) for high-viscosity oil and water, respectively. Also, figure A.8 depicts the numerical solutions of equation A.8 ($\partial p/\partial x \neq 0$) and equation 10 ($\partial p/\partial x = 0$) at four different times ($t = 1$s, 10s, 150s, and 3,500s and 2,400s) and $\phi = [0, \pi/2]$ for high-viscosity oil and water, respectively. Both numerical solutions are obtained with the same FD scheme. In all cases shown, the lines almost perfectly overlap, while the analytical solution sets a lower bound for the film thickness at initial times, and the van-der-Waals intermolecular force accelerates the drainage only when the film thickness is on the order of 100nm. It is interesting to study which of the two terms in the RHS of equation A.5 is dominant, which can be done through the film Eötvös number

$$Eo_{film} = \frac{\Delta p_g}{\Delta p_\sigma} = \frac{\rho g h}{\sigma \kappa} = \frac{\rho g h}{\sigma h''/(1 + h'^2)^{3/2}}. \tag{A.9}$$

For the three case studies of table 1, the Eo_{film} numerically calculated is such that $Eo_{film} \gg 1$ for $\phi \in [0, \pi/2]$ at every time, which means that the surface tension effects are negligible with respect to the hydrostatic term. As the film becomes thicker, the higher hydrostatic pressure opposes the liquid movement and reduces the film drainage, which explains why the film thickness values calculated with the analytical solution, equation 12, and the numerical solution of equation 10 are somewhat lower than those of the numerical solution of equation A.8. This makes the criterion to avoid film breakup, equation 15, slightly more conservative, which is valid for its purpose.

References

[1] Al-Safran, E.M., Gokcal, B., Sarica, C.. Investigation and prediction of high-viscosity liquid effect on two-phase slug length in horizontal pipelines. SPE Production & Operations 2013;28(03):296–305.

[2] Ansari, A.M., Sylvester, N.D., Sarica, C., Shoham, O., Brill, J.P.. A comprehensive mechanistic model for upward two-phase flow in wellbores. SPE Production & Facilities 1994;9(2):143–151.
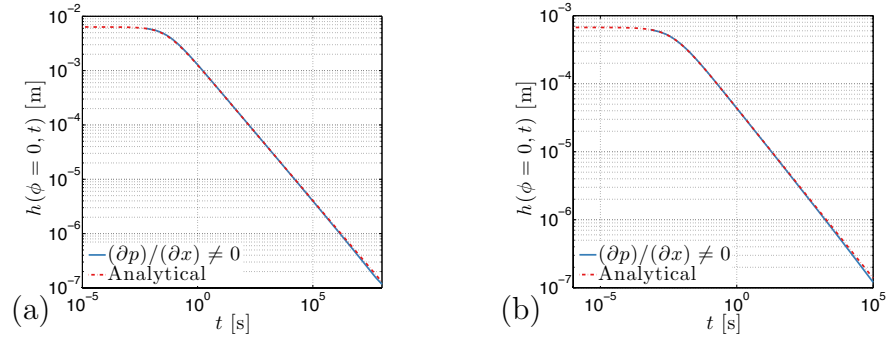
Figure A.7: Comparison of the numerical solution of equation A.8 where $\partial p/\partial x \neq 0$ and the analytical solution of equation 10 where $\partial p/\partial x = 0$ (equation 12) at $\phi = 0$ for high-viscosity oil (a) and water (b). Differences are negligible.
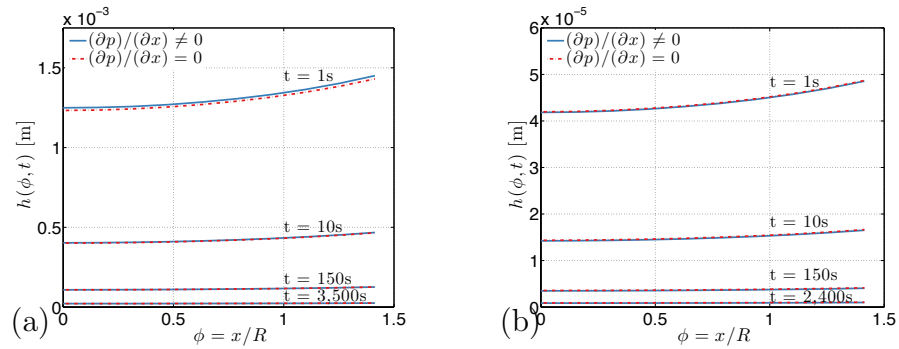

Figure A.8: Comparison of the numerical solution of equation A.8 ($\partial p/\partial x \neq 0$), and equation 10 ($\partial p/\partial x = 0$) at four different times ($t = 1s$, 10s, 150s, and 3,500s and 2,400s) and $\phi = [0, \pi/2]$ for high-viscosity oil (a) and water (b), respectively. Differences are negligible.

[3] Behafarid, F., Jansen, K.E., Podowski, M.Z.. A study on large bubble motion and liquid film in vertical pipes and inclined narrow channels. International Journal of Multiphase Flow 2015;75:288–299.

[4] Ben-Mansour, R., Sharma, A.K., Jeyachandra, B.C., Gokcal, B., Al-Sarkhi, A., Sarica, C.. Effect of pipe diameter and high oil viscosity on drift velocity for horizontal pipes. In: 7th North American Conference on Multiphase Technology. 2010. p. 237–248.

[5] Bird, J.C., Ruiter, R.D., Courbin, L., Stone, H.A.. Daughter bubble cascades produced by folding of ruptured thin films. Nature 2010;465(7299):759–762.

[6] Coriand, L., Rettenmayr, M., Duparré, A.. Relationship between the roughness and oleophilicity of functional surfaces. Advances in Contact Angle, Wettability and Adhesion, Volume Two 2015;165.

[7] Debrégeas, G., Gennes, P.G.D., Brochard-Wyart, F.. The life and death of "bare" viscous bubbles. Science 1998;279(5357):1704–1707.

[8] Delgado, M.. Classroom Note: The Lagrange–Charpit Method. SIAM Review 1997;39(2):298–304.

[9] Gokcal, B., Al-Sarkhi, A., Sarica, C., Al-Safran, E.. Prediction of slug frequency for high viscosity oils in horizontal pipes. SPE Annual Technical Conference and Exhibition 2009.

[10] Gregory, G.A., Scott, D.S.. Correlation of liquid slug velocity and frequency in horizontal cocurrent gas-liquid slug flow. AIChE Journal 1969;15(6):933–935.

[11] Hayashi, K., Kurimoto, R., Tomiyama, A.. Dimensional analysis of terminal velocity of a taylor bubble in a vertical pipe. Multiphase Science and Technology 2010;22(3):197–210.

[12] Hayashi, K., Kurimoto, R., Tomiyama, A.. Terminal velocity of a taylor drop in a vertical pipe. International Journal of Multiphase Flow 2011;37(3):241–251.

[13] Hernandez-Perez, V., Abdulkadir, M., Azzopardi, B.J.. Slugging frequency correlation for inclined gas–liquid flow. World Acad Sci, Eng Technol 2010;6:44–51.

19

[14] Hien, H.N., Fabre, J.. Test-case No 29a: The velocity and shape of 2D long bubbles in inclined channels or in vertical tubes (PA, PN) Part I: in a stagnant liquid. Multiphase Science and Technology 2004;16(1-3):177–189.

[15] Hien, H.N., Fabre, J.. Test-case No 29b: The velocity and shape of 2D long bubbles in inclined channels or in vertical tubes (PA, PN) Part II: in a flowing liquid. Multiphase Science and Technology 2004;16(1-3):191–206.

[16] Ishida, N., Sakamoto, M., Miyahara, M., Higashitani, K.. Attraction between hydrophobic surfaces with and without gas phase. Langmuir 2000;16(13):5681–5687.

[17] Ishida, N., Sakamoto, M., Miyahara, M., Higashitani, K.. Optical observation of gas bridging between hydrophobic surfaces in water. Journal of Colloid and Interface Science 2002;253(1):112–116.

[18] Israelachvili, J.N.. Intermolecular and surface forces: revised third edition. Academic Press 2011.

[19] Kamura, A., Takata, Y., Hazuku, T., Fukuhara, Y., Takamasa, T.. Temperature dependence of surface wettability before and after γ-ray irradiation. Proceedings of the 13th international topical meeting on nuclear reactor thermal hydraulics (NURETH-13) 2009.

[20] Kurimoto, R., Hayashi, K., Tomiyama, A.. Terminal velocities of clean and fully-contaminated drops in vertical pipes. International Journal of Multiphase Flow 2013;49:8–23.

[21] Lizarraga-Garcia, E., Buongiorno, J., Al-Safran, E., Lakehal, D.. CFD-informed unified closure relation for the rise velocity of Taylor bubbles in pipes. Bulletin of the American Physical Society 2015;60.

[22] Lizarraga-Garcia, E., Buongiorno, J., Al-Safran, E., Lakehal, D.. Development of a new CFD-based unified closure relation for Taylor bubble velocity in two-phase slug flow in pipes. In: 17th International Conference on Multiphase Production Technology, Cannes, France. BHR Group; 2015.

[23] Llewellin, E.W., Bello, E.D., Taddeucci, J., Scarlato, P., Lane, S.J.. The thickness of the falling film of liquid around a Taylor bubble. Proceedings of the Royal

20

Society A: Mathematical, Physical and Engineering Science 2012;468(2140):1041–1064.

[24] Lou, S., Gao, J., Xiao, X., Li, X., Li, G., Zhang, Y., Li, M., Sun, J., Li, X., Hu, J.. Studies of nanobubbles produced at liquid/solid interfaces. Materials Characterization 2002;48(2):211–214.

[25] Maneri, C.C., Zuber, N.. An experimental study of plane bubbles rising at inclination. International Journal of Multiphase Flow 1974;1(5):623–645.

[26] Manev, E.D., Nguyen, A.V.. Critical thickness of microscopic thin liquid films. Advances in Colloid and Interface Science 2005;114:133–146.

[27] MATLAB®, version 8.2.0.701 (R2013b). Natick, Massachusetts: The Math-Works Inc., 2013.

[28] Mysels, K.J., Shinoda, K., Frankel, S.. Soap films: studies of their thinning and a bibliography. Pergamon Press 1959.

[29] Nguyen, A., Schulze, H.J.. Colloidal science of flotation. CRC Press 2003.

[30] Orell, A., Rembrand, R.. A model for gas-liquid slug flow in a vertical tube. Industrial & Engineering Chemistry Fundamentals 1986;25(2):196–206.

[31] Oron, A., Davis, S.H., Bankoff, S.G.. Long-scale evolution of thin liquid films. Reviews of Modern Physics 1997;69(3):931.

[32] Petalas, N., Aziz, K.. A mechanistic model for multiphase flow in pipes. Journal of Canadian Petroleum Technology 2000;39(6):43–55.

[33] Podowski, M., Hirsa, A.. The effect of nanoparticles on taylor-bubble motion in inclined pipes. 4th International Conference on Multiphase Flow 2001;1.

[34] Podowski, M.Z., Kumbaro, A.. The modeling of thin liquid films along inclined surfaces. Journal of Fluids Engineering 2004;126(4):565–572.

[35] Reisfeld, B., Bankoff, S.G.. Non-isothermal flow of a liquid film on a horizontal cylinder. Journal of Fluid Mechanics 1992;236:167–196.

21

[36] Ruckenstein, E., Jain, R.K.. Spontaneous rupture of thin liquid films. Journal of the Chemical Society, Faraday Transactions 2: Molecular and Chemical Physics 1974;70:132–147.

[37] Schulze, H.J.. Physico-chemical elementary processes in flotation. Elsevier, Amsterdam 1984.

[38] Schulze, H.J., Stöckelhuber, K.W., Wenger, A.. The influence of acting forces on the rupture mechanism of wetting films–nucleation or capillary waves. Colloids and Surfaces A: Physicochemical and Engineering Aspects 2001;192(1):61–72.

[39] Sheludko, A.. Advances in colloid and interface science. Vol 1 Elsevier, Amsterdam 1967;391.

[40] Stöckelhuber, K.W.. Stability and rupture of aqueous wetting films. The European Physical Journal E: Soft Matter and Biological Physics 2003;12(3):431–435.

[41] Stöckelhuber, K.W., Radoev, B., Wenger, A., Schulze, H.J.. Rupture of wetting films caused by nanobubbles. Langmuir 2004;20(1):164–168.

[42] Taha, T., Cui, Z.F.. CFD modelling of slug flow in vertical tubes. Chemical Engineering Science 2006;61(2):676–687.

[43] Taitel, Y., Dukler, A.E.. A model for predicting flow regime transitions in horizontal and near horizontal gas-liquid flow. AIChE Journal 1976;22(1):47–55.

[44] Tyrrell, J.W.G., Attard, P.. Images of nanobubbles on hydrophobic surfaces and their interactions. Physical Review Letters 2001;87(17):176104.

[45] Tyrrell, J.W.G., Attard, P.. Atomic force microscope images of nanobubbles on a hydrophobic surface and corresponding force-separation data. Langmuir 2002;18(1):160–167.

[46] Viana, F., Pardo, R., Yanez, R., Trallero, J.L., Joseph, D.D.. Universal correlation for the rise velocity of long gas bubbles in round pipes. Journal of Fluid Mechanics 2003;494:379–398.

[47] Vrij, A.. Possible mechanism for the spontaneous rupture of thin, free liquid films. Discussions of the Faraday Society 1966;42:23–33.

22

330 [48] Zabaras, G.J.. Prediction of slug frequency for gas/liquid flows. SPE Journal 2000;5(03):252–258.